UCRL- 83519
PREPRINT

STUDIES IN TANDEM MIRROR THEORY

D. E. Baldwin, R. H. Cohen, T. B. Kaiser
B. G. Logan, L. D. Pearlstein, M. Porkolab,
and M. E. Rensink

This paper was prepared for submittal to

8th International Conference on Plasma Physics
and Controlled Nuclear Fusion Research

Brussels, Belgium

1-10 July 1980

May 23, 1980

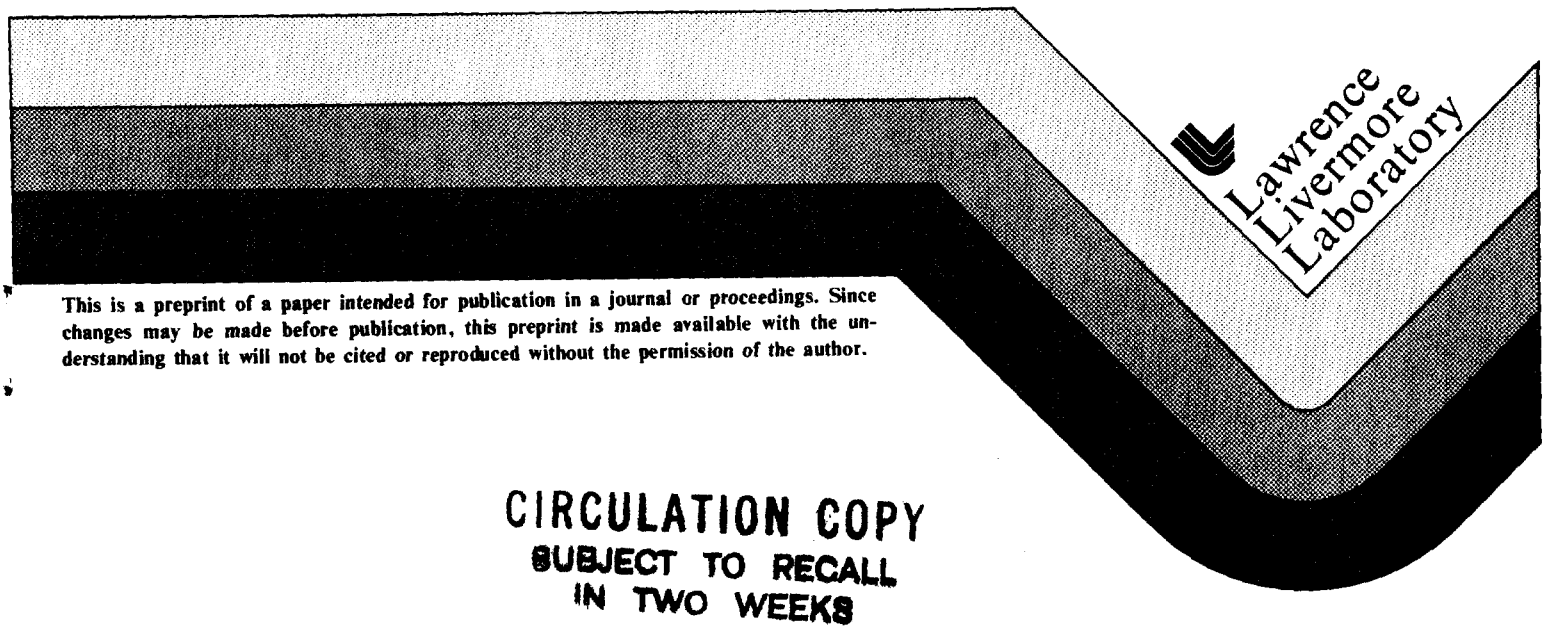

INTERNATIONAL ATOMIC ENERGY AGENCY

8th INTERNATIONAL CONFERENCE ON PLASMA PHYSICS AND CONTROLLED NUCLEAR FUSION RESEARCH

Brussels, 1–10 July 1980

IAEA-CN-38/ F-4

STUDIES IN TANDEM MIRROR THEORY

D. E. BALDWIN, R. H. COHEN, T. B. KAISER,
B. G. LOGAN, L. D. PEARLSTEIN, M. PORKOLAB,*
and M. E. RENSINK

Lawrence Livermore National Laboratory,
University of California,
Livermore, California, U.S.A. 94550

*Permanent address: MIT, Cambridge, MA, U.S.A.

IAEA-CN-38/F-4

STUDIES IN TANDEM MIRROR THEORY

ABSTRACT

This paper discusses the formation, maintenance, and microstability of thermal barriers, which have been introduced as a means for improving tandem mirror reactor performance at reduced technological demands. It also describes calculations of tandem mirror central-cell β limits due to MHD ballooning modes.

1. THERMAL BARRIERS

1.1 Introduction

Thermal barriers (TB's) [1] are intended to improve the performance and reduce the technology requirements of a tandem mirror (TM) fusion device. Theoretically, they also generate ion velocity and space distributions that are stable to the loss-cone instabilities common to mirror machines. Making use of the TB concept requires only modification of conventional TM designs and does not require new components or technologies. Although the basic principles of barriers have antecedents in a variety of mirror experiments, tests of their feasibility await experiments now under construction at Lawrence Livermore National Laboratory (LLNL) and elsewhere.

Calculations show [2] that a TM reactor would require central-cell ion and electron temperatures $T_c \approx T_{ec} \approx 40$ keV and a plugging potential seen by the central cell $\phi_c \approx 100$ kV. When the distribution of electrons along the magnetic field is described by a Boltzmann distribution, these imply a ratio of plug-to-central cell density $n_p/n_c \approx 9$, in turn implying high magnetic fields and injection energies for the plugs. Using auxiliary electron heating to increase $\phi_c \propto T_{ec}$ is most effective only when T_{ec}/T_c is increased (otherwise, the central-cell confinement parameter $n\tau_c \approx 7 \times 10^{10}\ T_c^{3/2}\ (\phi_c/T_c)\ \exp(\phi_c/T_c)$ increases only as $T_c^{3/2}$), and large increases in the ratio T_{ec}/T_c are precluded by ion-electron coupling in the central cell.

The essential idea of thermal barriers is to raise the electron temperature in the potential peak T_{ep} relative to T_{ec} and T_c, since ϕ_c scales approximately with T_{ep}. Because in a conventional TM the central-cell electrons pass through the plugs, their power transfer with those trapped in the plugs is sufficient to prevent establishment of a significant temperature difference in spite of intense plug-electron heating. As seen from the central cell, a thermal barrier is a negative dip in potential before the positive peak of the plugging potential. It restricts the flow of low-energy electrons from the central cell to the potential peak, thereby reducing their thermal coupling and allowing an increase in T_{ep} with auxiliary heating. This negative dip in potential is created by

maintaining a relative minimum in ion density, just as the potential peak is generated by a relative ion-density maximum.

Two experiments are under construction at LLNL incorporating TB's. Their designs differ in the combination of the barrier/plug configuration and the additional requirement of magnetohydrodynamic (MHD) flute-interchange stability (see Fig. 1a). Both employ regions of high-pressure plasma in quadrupole-stabilized mirrors to anchor the central cells. The TM conversion of the Mirror Fusion Test Facility (MFTF), MFTF-B, splits these functions by providing the MHD anchor and the barrier/plug in two successive mirror cells at each end of the central cell, respectively, a yin-yang and a fan-shaped mirror region called an A-cell. The TMX upgrade combines these functions into a single minimum-B mirror cell at each end, superficially like a conventional TM, but neutral beams are injected differently.

1.2 Barrier formation

The TMX upgrade end cell is an elongated, quadrupole-stabilized mirror machine having a β-enhanced mirror ratio ≈ 4, and the axial B profile as shown in Fig. 1b, in which the central cell lies to the left. (In the MFTF-B, the axial B profile in the A-cell is similar, although the yin-yang cell and its pressure peak for MHD stability would like to the left.) Ions are injected either normal to $\underset{\sim}{B}$ at $B/B_b \approx 2$, or at 45° to $\underset{\sim}{B}$ at the midplane. Such injection causes a peaking in the ion density at the turning points in what is termed a sloshing-ion distribution having two maxima, or lobes. Collisional relaxation of this double-peaked density profile is prevented by removing ions scattering to large pitch angles by charge exchange on the injected beams, supplemented as necessary by axially injected "pump beams." Pump beams, injected into the loss cone of the mirrors, remove trapped ions by charge exchange, converting them into passing ions, thereby reducing departures from the injection profile. Sample Fokker-Planck-determined profiles are given in Sec. 1.3.

The flow of ions entering the mirror from the central cell is throttled by the first mirror, expands in the decreasing magnetic field, and finally is reflected by the potential ϕ_c described below. To the left of point b in Fig. 1b, the potential and density satisfy Boltzmann's relation, so that this decreasing density, together with the density depression in the sloshing-ion profile, generates a barrier between the outer lobe of density and the inner-lobe-central-cell region. When electrons trapped in the outer lobe are heated by local application of electron cyclotron resonance heating (ECRH), T_{ep} and the outer lobe potential will rise to generate the ϕ profile shown in Fig. 1b. The potential peak at point p forms the final plug as seen by the central cell. Energetic, anisotropic electrons that are magnetically trapped and result in part from the heating in the outer lobe and in part from a second ECRH frequency tuned to the midplane

electron gyrofrequency will depress the thermal electron density at the barrier midplane n_b^* below the ion density n_b.

Two important results have been obtained by Cohen et al. [3]. The potential $\phi_b + \phi_c$ adjusts so that the net particle flux between locally trapped and passing electrons nearly vanishes, matching only that injected by ionization of neutral beams. For parameters of interest, they find

$$\phi_c + \phi_b = T_{ep} \ln \left[\left(n_p/n_b^* \; T_{ec}/T_{ep} \right)^{1/2} \right] , \tag{1}$$

or

$$\phi_c = T_{ep} \ln \left[\left(n_p/b_b^* \right) \left(T_{ec}/T_{ep} \right)^{1/2} \right] - T_{ec} \ln \left(n_c/n_b^* \right) \tag{2}$$

For sufficiently low n_b^* and large T_{ep}/T_{ec}, the required ϕ_c can be generated by an ion density n_p even less than n_c.

For the power transfer they found [3]

$$P_e = - n_p (T_{ep} - T_{ec}) \; \tau_p^{-1} \; (1 + g(R)/2R) \quad , \tag{3}$$

where $\tau_p = \sqrt{\pi/4} \, \tau_0 \; g(R) \, \xi \exp(\xi)$ when $\xi = (\phi_b + \phi_c)/T_{ep} \geq 2$, and τ_0 is the electron-electron scattering time, and $g(R) \approx 1$; for $R >> 1$, $g(R) = W \ln \left[(W + 1)/(W - 1) \right]$ with $W = (1 + R^{-1})^{1/2}$. Equating this power to the ECRH power applied to the outer lobe determines T_{ep}.

Detailed variation of $\phi(z)$ is determined from charge neutrality. When densities are calculated from model distribution functions having discontinuities, discontinuous potential profiles can result. However, distributions that model properly smooth Fokker-Planck solutions yield continuous profiles, such as that shown in Sec. 1.3.

Studies of the energetics of this configuration show that the large reduction in ion density required to sustain ϕ_c, compared to a TM without barriers, results in saving more power than is expended in maintaining the barrier profiles, including the pumping and ECRH [5].

1.3 Fokker-Planck solutions

The sloshing-ion end cell distributions described in the preceding section have been obtained by numerical integration of a bounce-averaged Fokker-Planck equation of the form

$$\frac{\partial f}{\partial t}\oint \frac{dz}{v} = \oint \frac{dz}{v_{\parallel}} \left\{ \left.\frac{\partial f}{\partial t}\right|_{coll.} + \sum_b \left[n_i(\nu_{Ib} + \nu_{xb})\, S_b(z,v) - \nu_{xs} f \right] \right\} , \quad (4)$$

where ν_{Ib} and ν_{xb} are the ionization and charge-exchange rates, and $S_b(z,v)$ is the ion source shape associated with the b^{th} neutral beam. Wells of arbitrary shape, even in z, are allowed. Ion density profiles $n_i(z)$ are calculated from the solution f, which is a function of constants of the bounce motion; and assuming Maxwellian electrons, we find the ambipolar profile from

$$\phi(z) = \phi(0) + T_e \ell n\left[n_i(z)/n_i(0)\right] , \quad (5)$$

where "0" refers to the midplane. Ion density profiles $n_i(z)$ peaked off midplane similarly generate potentials peaked off midplane. In this symmetric model, these potentials are not asymmetric as shown in Fig. 2a; rather, by proper choice of T_e, both sides have the higher peak of the figure.

We find that sloshing-ion distributions result over a wide range of system parameters, if injection is localized at a magnetic field >1.3 times the midplane field and charge-exchange removal of ions scattering out of the injection profile is sufficient. A profile generated in a mirror ratio well of $R_m = 4$ by injection normal to $\underset{\sim}{B}$ at $B(inj) = 2.5\ B_0$ is shown in Fig. 2a; a similar profile would result for injection at $\theta(inj) = 40^o$ at the midplane. For normal injection away from the midplane, charge-exchange pumping requires a second beam injected at small pitch angle; for angled injection at the midplane, charge exchange on the beam usually suffices. For the example in Fig. 2a, the averaged ratio of charge exchange to ionization was $\dot{n}_{cx}/\dot{n}_{ion} = 1/2$. Similar distributions were obtained for R_m varying from 3 to 6.5, $\theta(inj)$ from 40^o to 65^o, $\dot{n}_{cx}/\dot{n}_{ion}$ from 1/2 to 6/7, and electron temperature injection energy from 0.01 (drag-dominated) to 0.5 (no drag). Distribution functions for MFTF-B and TMX upgrade parameters will have much more low energy component, corresponding to a passing ion density roughly equal to the sloshing ion density. In some cases, f is nearly monotonic in $v_\perp$.

1.4 Microstability of the sloshing-ion distribution

The non-Maxwellian distributions characteristic of sloshing ions in the end cells are far more stable to familiar mirror loss-cone-type instabilities than those having the density maximum at the field minimum. The passing and barely trapped ions partially fill the low-$v_\perp$ region below the peak of the sloshing ions. We employ the model

$$f_\perp(v_\perp) = \frac{\eta_i}{\ell! v_1^2}\left(\frac{v_\perp^2}{2v_1^2}\right)\exp\left(-\frac{v_\perp^2}{2v_1^2}\right)$$

$$+\frac{1-\eta_i}{v_2^2}\exp\left(-\frac{v_\perp^2}{2v_2^2}\right), \qquad (6)$$

where ℓ is a positive integer, and the parameters ℓ, v_1^2, v_2^2, and η_i are adjusted to best fit the Fokker-Planck results. For Fig. 2b, take $\ell = 4$, $v_1 = v_2$, and $\eta_i = 0.9$.

We calculate stability to loss-cone modes using a differential equation along B that treats variation across B in an eikonal approximation [6]. Previous results found the DCLC mode at $\omega = \Omega_{ci}$ (midplane) to be stabilized by a warm-plasma density fraction $\geq 5\%$ at the midplane. For the sloshing-ion barrier plugs described, the passing ions (low $v_\perp$ in Fig. 2b) exceed this fraction for all parameters of interest. The only remaning modes found are higher harmonic, shorter wavelength modes [7] that can localize in the outer density lobe in Fig. 1b. For stability these require more filling of the low-v distribution, $\eta_i \approx 0.5$ in Eq. (6), corresponding to a passing ion density roughly equal to the trapped ion density, as in MFTF-B and TMX upgrade.

A second drive for instability lies in the streaming-ion character of the $v_\parallel$-distribution, which we model by drifting Maxwellians having temperature $T_{i\parallel}$ and drift energy E_{drift}. To analyze this stability, we treat the electrons adiabatically, allowing for a fraction η_e of anisotropic electrons having $T_{e\perp}$ and $T_{e\parallel}$ and treat ions allowing finite $k_\perp \rho_i$, although generally $k_\perp \rho_i >> 1$ is most severe. Absolute modes having $\mathrm{Re}\,\omega = 0$ require max $D(k_\parallel, k_\perp) \geq 0$, generating the stability boundary shown in Fig. 3. The percentages in Fig. 3 show fractions η_e for MFTF-B parameters. Introduction of hot electrons to enhance the barrier effect by reducing n_b^* in Eq. (2) is destabilizing and would place at least an upper bound on this hot-electron fraction. For the same reason, we expect the barrier midplane, where the hot electron density is maximum, to be the most susceptible to these modes.

Modes having $\mathrm{Re}\,\omega \neq 0$ are being examined by a Nyquist analysis. However, these are expected to place less severe constraints than those with $\mathrm{Re}\,\omega = 0$.

Alfvén waves, which otherwise might be unstable when $u_b \gtrsim V_A$ (the Alfvén speed), are stabilized by the presence of the hot, mirror-trapped electron anisotropy ($v_{e\perp}^2 - v_{e\parallel}^2$). The shear and compressional Alfven modes, respectively, are given by

$$\omega^2 = k^2 V_A^2 + \left[2k^2 T_{e\perp} + k_\parallel^2 (T_{e\perp} - T_{e\parallel})\right]/M_i \qquad (7)$$

and

$$\omega^2 = k_\parallel^2 \left[V_A^2 + (T_{e\perp} - T_{e\parallel})/M_i \right] \qquad (8)$$

so that $\omega/k_\parallel = 0(T_e/M_i)^{1/2}$, too fast to couple to the drifting ions. A similar statement holds regarding the effect of these electrons on the firehose condition, $B^2 + 4\pi(P_\perp - P_\parallel) > 0$.

2. BALLOONING MODES

The maximum β achievable is thought to be limited by ballooning modes satisfying an eigenmode equation derived from a large-aspect-ratio expansion of the guiding-center energy principle [8,9]. For a tandem with TB's the parameter space available has six degrees of freedom: the field line coordinates ψ and θ, the angle specifying the orientation of the wave vector, and the values of β in the central, yin-yang, and barrier cells, β_c, β_p, and β_b, respectively. The lowest eigenvalue ω_0^2 lies near the surface in the symmetry plane, and has only ψ displacement, satisfying

$$\frac{d}{dz}\left[\mathscr{E}^2 \frac{Q}{B^2}\frac{dV}{dz}\right] + \left[\omega^2 \frac{\mathscr{E}^2}{V_A^2} + \frac{4\pi\psi}{B}\frac{\partial(P_\perp + P_\parallel)}{\partial\psi} K_\psi\right] V = 0 \quad , \qquad (9)$$

where $\mathscr{E}^2$ is the flux-surface ellipticity, K_ψ is the normal curvature, and $QB^{-2} = 1 + 4\pi(P_\perp - P_\parallel)/B^2$. The parameter space is that of the β's only.

The effect of the various terms in Eq. (9) on stability can be seen in the variational form

$$\omega^2 \alpha \int dz \left[\mathscr{E}^2 \frac{Q}{B^2}\left(\frac{dV}{dz}\right)^2 + \left|\frac{\partial(P_\perp + P_\parallel)}{\partial\psi}\right| \frac{4\pi\psi}{B} V^2\right] .$$

The first term, the line bending/stretching term, is positive-definite and stabilizing. If $\mathscr{E}^2 << 1$ anywhere along the flux tube, dV/dz can be large (the flux tube can bend and stretch) without a large stabilizing effect. The second term is locally stabilizing or destabilizing, depending on the sign of K_ψ. If regions of positive and negative curvature are separated by a region of $\mathscr{E}^2 << 1$, the mode can localize to minimize good curvature and maximize bad curvature, having only a small expenditure of bending/stretching energy.

Eigenmodes having just such a structure are found in numerical solutions of Eq. (9). An example is shown in Fig. 4a, where plots of the two terms in the integrand of Eq. (9) are superimposed on one of the eigenmode amplitude.

The calculated stability boundaries for MFTF-B, $\min \omega_0^2 = 0$, are shown in Fig. 4b for two values of β_b. The system is stable (unstable) to the left (right) of each curve.

ACKNOWLEDGMENT

This work was performed under the auspices of the U. S. Department of Energy by the Lawrence Livermore National Laboratory under contract number W-7405-ENG-48.

REFERENCES

[1] BALDWIN, D. E., LOGAN, B. G., Phys. Rev. Lett. 43 (1979) 1318; see also Physics Basis for MFTF-B, Lawrence Livermore National Laboratory, CA, BALDWIN, D. E. LOGAN, B. G., and SIMONEN, T. C., Eds. UCID-18496 (1980).

[2] CARLSON, G. A., et al., Lawrence Livermore National Laboratory, Livermore, CA Rpt. UCID-18158 (1979).

[3] COHEN, R. H., et al., submitted to Nucl. Fusion, Lawrence Livermore National Laboratory, Livermore, CA Rpt. UCRL-84147 (1980).

[4] COHEN, R. H., et al., Nucl. Fusion 18 (1978) 1229; COHEN, R. H., Nucl. Fusion 19 (1979) 1693 and 19 (1979) 1295.

[5] CARLSON, G. A., et al., Lawrence Livermore National Laboratory, Livermore, CA Rpt. UCRL-52836 (1979).

[6] BERK, H. L., et al., Plasma Phys. Cont. Nucl. Fusion Res. (Proc. 6th Int. Conf. Berchtesgaden, 1976) Vol. 3, IAEA, Vienna (1977) 147.

[7] GERVER, M. J., Phys. Fluids 23 (1980) 755.

[8] NEWCOMB, W. A., Lawrence Livermore National Laboratory, Livermore, CA Rpt. UCID-17182 (1976).

[9] BALDWIN, D. E., et al., Plasma Phys. Cont. Nucl. Fusion Res. (Proc. 7th Int. Conf. Innsbruck, 1978) (1979) IAEA, Vienna (1979) II, 427.

FIGURE CAPTIONS

Fig. 1a Schematic diagrams of (top) the MFTF-B and (bottom) the TMX Upgrade magnet configuration. For simplicity two circular coils are not shown on the TMX-Upgrade.

1b Profiles of magnetic field B, potential θ, and density n vs z for barrier/plug end-cell with sloshing ions.

Fig. 2a Axial profiles of density and magnetic field for sloshing-ion example. E(inj) = 80 keV, R(inj) = 2.5 at 125 cm, $R_m = 4$, potential = 40 kV, T_{ep} = 40 kev, and T_c = 15 TeV.

2b $v_\perp$, $v_\parallel$-distributions at the midplane of example a.

Fig. 3 Stability boundary for ion-ion, $\mathrm{Re}\omega = 0$ mode for a distribution modelling the Fokker-Planck solution. Percents refer to hot-electron fraction in MFTF-B.

Fig. 4a Axial structure of a typical ballooning eigenmode in a tandem with A-cell thermal barriers. Plots of the line-bending and curvature coefficients are also shown.

4b Ballooning-mode marginal-stability boundaries in a tandem with A-cell thermal barriers for two different values of β_b.

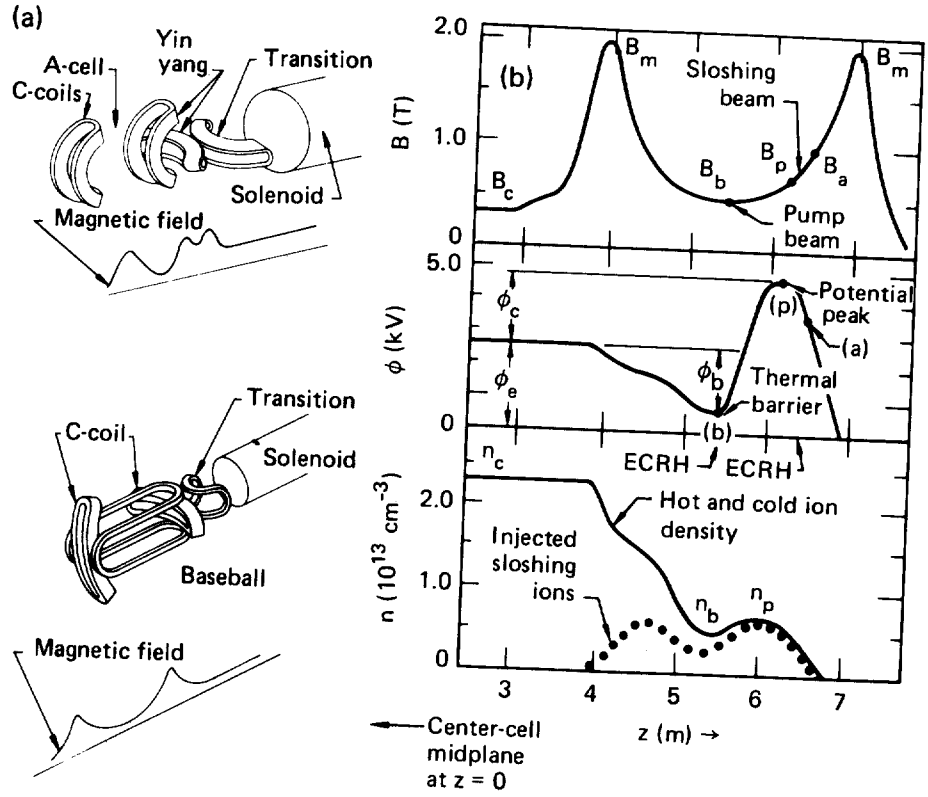

Fig. 1a. Schematic diagrams of (top) the MFTF-B and (bottom) the TMX Upgrade magnet configuration. For simplicity two circular coils are not shown on the TMX Upgrade.

Fig. 1b. Profiles of magnetic field B, potential θ, and density n vs z for barrier/plug end-cell with sloshing ions.

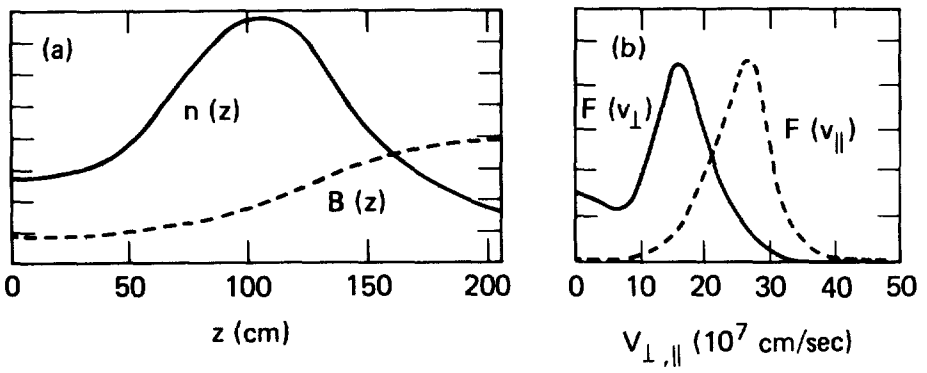

Fig. 2a. Axial profiles of density and magnetic field for sloshing-ion example. E(inj) = 80 keV, R(inj) = 2.5 keV, and T_c = 15 TeV.

Fig. 2b. $v_\perp$, $v_\parallel$-distributions at the midplane of example a.

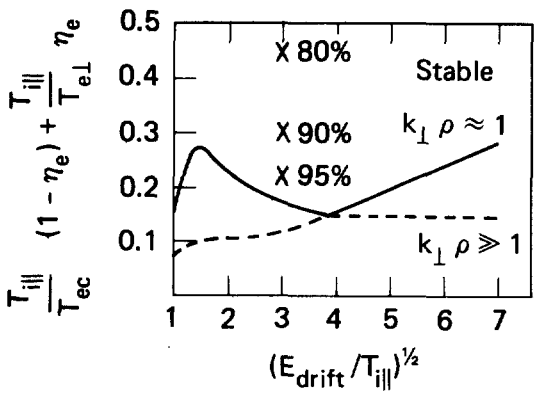

Fig. 3. Stability boundary for ion-ion, Reω = 0 mode for a distribution modelling the Fokker-Planck solution. Percents refer to hot-electron fraction in MFTF-B.

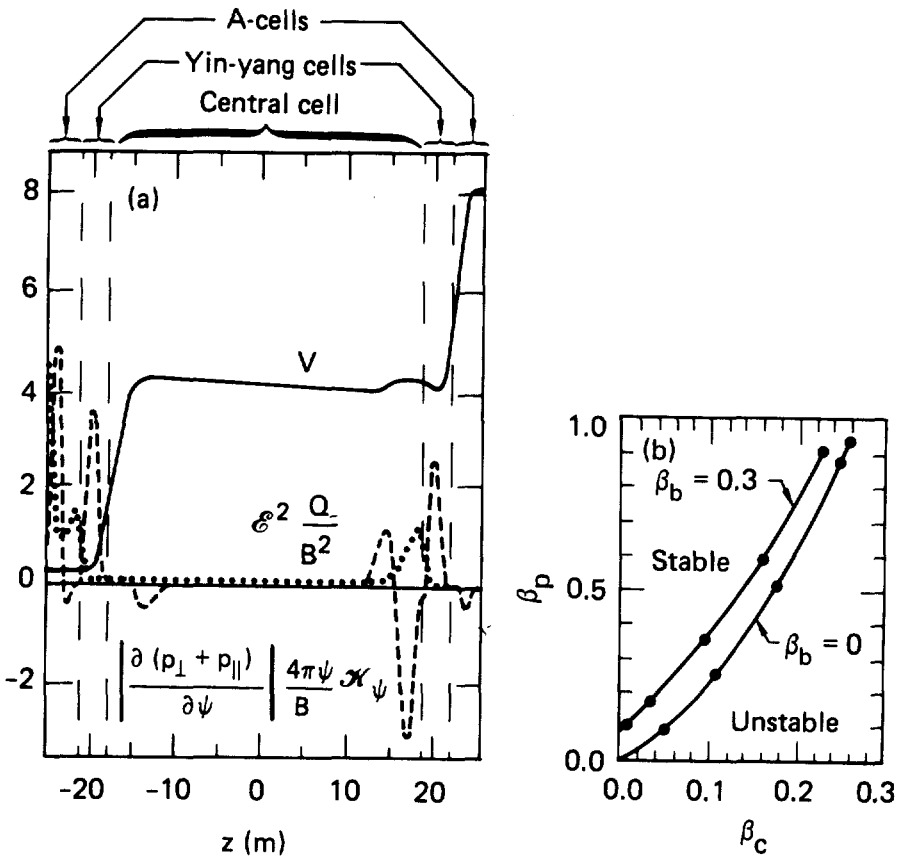

Fig. 4a. Axial structure of a typical ballooning eigenmode in a tandem with A-cell thermal barriers. Plots of the line-bending and curvature coefficients are also shown.

Fig. 4b. Ballooning-mode marginal-stability boundaries in a tandem with A-cell thermal barriers for two different values of β_b.